Ocean Engineering 126 (2016) 138–151

Contents lists available at ScienceDirect

Ocean Engineering

journal homepage: www.elsevier.com/locate/oceaneng

Rigid-flexible-cavity coupling trajectory and uncertainty trajectory analysis of supercavitating projectiles

Ling Zhou *, Yanhui Li, Zhipeng Xue, Jingzhuang Han, Nan Zhang

Department of UAV, Changchun Institute of Optics, Fine Mechanics and Physics, Chinese Academy of Sciences, Changchun City 130033, PR China

ARTICLE INFO

Article history:
Received 24 January 2016
Received in revised form
13 June 2016
Accepted 27 August 2016
Available online 13 September 2016

Keywords:
Supercavitating projectiles
Rigid-flexible-cavity coupling trajectory
Uncertainty trajectory
Chaos method
Random variables
Non-probabilistic interval variables

ABSTRACT

Structures of supercavitating projectiles operating at high underwater velocity are subjected to large deformations generated by high forces acting on the projectile. Moreover, it is widely that probabilistic and non-probabilistic uncertain information are coexisting. Therefore, flexible and uncertainty trajectory analysis of supercavitating projectiles are required. Formulae of flexible body motion and rigid-flexible coupling dynamic differential equations are introduced first. Then rigid-flexible coupling equations are decoupled. Flexible deformations are solved by modal superposition method; detailed rigid trajectory equations in vertical plane, supercavity equation and force formulae are presented, and calculation flowchart of rigid-flexible-cavity coupling trajectory is given. Third, by chaos method, the uncertainty rigid-flexible-cavity coupling trajectory simulation of supercavitating projectiles with uncertain launch parameters is performed, and parameters are described by random variables and non-probabilistic interval variables. Finally, The correctness of rigid-flexible-cavity coupling trajectory algorithm is validated by the experimental data provided by relevant literatures. To investigate the effect of flexible deformation of projectile on coupling trajectory, the variation of the resultant coupling trajectory was investigated by varying two important flexibility parameters – slenderness ratio and Young's modulus. The results of rigid-flexible-cavity coupling trajectory are compared with that of rigid-cavity trajectory through an engineering example. Trajectory curves sets and distribution of impact points are presented through uncertainty rigid-flexible-cavity coupling trajectory simulation.

1. Introduction

The local pressure of a fluid decreases as the bodies move at sufficient high speed through water, and then low-density gas generates. The gas forms a cavity, which envelops the moving body according to a phenomenon commonly known as “supercavity” (Ashley, 2001). Supercavitating bodies can reach high speeds in water, such as the speed of a supercavitating projectile used in experiments is approximately 1500 m/s (Harkins, 2001). To meet the requirements of fluid dynamics enveloped by a supercavity, supercavitating projectiles are usually designed as slender bodies. However, the high slenderness ratio combined with the large axial force caused by the cavitator drag and the sliding force, which are proportional to the square of velocity, may easily cause large deformations of structure in the supercavitating projectiles. Therefore, when performing trajectory analysis of supercavitating projectiles, large deformations of structure need to be considered.

At present, researches on the supercavitating vehicles mainly focus on hydrodynamics, control, and buckling problems (Semenenko, 2004; Zhang et al., 2015; Ruzzene, 2004) and only a few trajectory analysis, especially flexible trajectory calculation and uncertainty trajectory analysis of supercavitating vehicles, have been carried out. Kulkarni and Pratap (2000) studied the rigid dynamics of a supercavitating projectile. Rand et al. (1997) investigated the in-flight dynamics of a simplified model of a supercavitating body, Ruzzene et al. (2008) and evaluated the optimal rigid-cavity coupling trajectories for supercavitating vehicles. Choi et al. (2004) used Modal-Based Elements to perform dynamic analysis of flexible supercavitating vehicles. The dynamic behaviour of supercavitating underwater vehicles and the vibration in supercavitating underwater vehicles were investigated and controlled by Ruzzene and Soranna (2004). Cavity formula and sliding force formula reported in Choi et al. (2004) and Ruzzene and Soranna (2004), do not take into account the unsteady supercavity characteristics, and the value of the constant in sliding force formula should be obtained by experiments.

Nonetheless, the parameters are commonly uncertain in engineering, so deterministic trajectory analyses are not adequate. Commonly there are uncertain factors in initial launch process, which will effect on the resulting trajectory. For example, the

* Corresponding author.
E-mail address: hszl007@163.com (L. Zhou).

http://dx.doi.org/10.1016/j.oceaneng.2016.08.032
0029-8018/

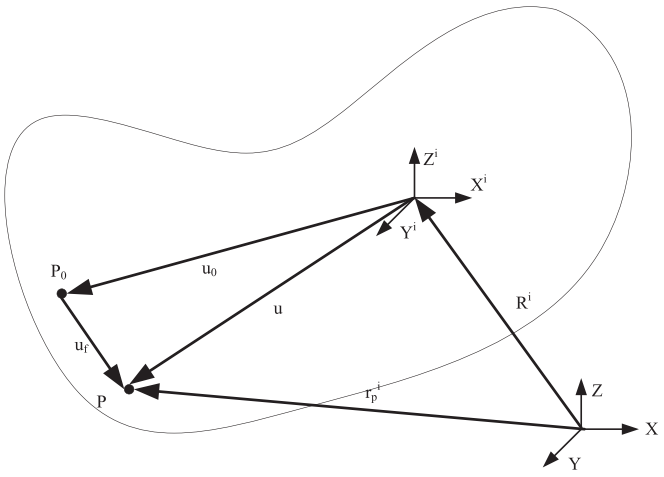

Fig. 1. Flexible body dynamic.

initial velocity of the launch, initial angular velocity and pitch angle are not determined in supercavitating projectile's launch process. Due to disturbances generated during launch by manufacturing errors of supercavitating projectiles and by launch equipment, flow disturbances, and launch equipment pressure disturbances the above-mentioned initial launch parameters are uncertain. Jiang performed trajectory stochastic characteristics analysis of supercavitating projectile with stochastic parameters (Yunhua et al., 2011), but the flexible characteristic of vehicle was not considered and the distributions of random variables were infinite. However, truncated random variables should be used instead of continuous random variables for practical engineering applications because most of random variables are bounded (Xiao et al., 2014).

Besides truncated random variables, there are non-probabilistic interval variables, and it is common that the above two uncertainties are coexisting because there are many uncertain variables with various data samples and various characteristics in engineering. For example, uncertain variables can be described as random variables when data samples are adequate and an accurate probability distribution can be obtained. However, an accurate probability distribution cannot be obtained with a too small sample of data. Small changes in the probability distribution of uncertain variables can generate large differences in the probabilistic analysis results (Elishakoff, 1995). Therefore, uncertainty variables cannot be treated as random variables when their sample data are too few to obtain accurate probabilistic analysis results. However, the boundaries of uncertain variables may be easily obtained from engineers and test data. Therefore, the use of a non-probabilistic interval variable to describe uncertain variables is appropriate (Ben-Haim, 1994).

According to the above analysis, flexible characteristics of supercavitating projectile, unsteady supercavity, and uncertainties of the launch parameters must be considered. Therefore, it is necessary to perform uncertainty rigid-flexible-cavity coupling trajectory analysis of supercavitating projectiles.

In this paper, rigid-flexible-cavity coupling trajectory and uncertainty trajectory analysis of supercavitating projectiles are presented. The unsteady supercavity characteristics, directional effect of cavitator and floating deformation of cavity tail will be considered and a more accurate calculation formula of sliding lift force will be used. The paper is organized as follows. Flexible body motion analysis and rigid-flexible coupling equations are presented in Section 2. Rigid-flexible coupling equations are decoupled, and flexible deformations are solved by modal superposition method in Section 3. Detailed rigid trajectory equations in vertical plane, supercavity equations, force formulae and solving flowcharts are presented in Section 4. Uncertainty variables are generated by chaotic variables and simulation flowcharts of uncertain trajectory are presented in Section 5. In Section 6, numerical examples of supercavitating projectiles and main results are presented. Finally, conclusions are drawn in Section 7.

2. Flexible body motion analysis

In Fig. 1, *XYZ* is a global coordinate system, and *XiYiZi* is a body coordinate system, so the global coordinate of arbitrary point P on the body is expressed as

$$r_p^i = R^i + A^i u \tag{1}$$

where, R^i is position vector of body in global coordinate system, A^i is rotation matrix from local coordinate system to global coordinate system, u is position vector of point P in local coordinate system. Flexible deformations were considered and u could be expressed as

$$u = u_0 + u_f \tag{2}$$

where, u_0 and u_f are undeformed position vectors and deformation displacement vectors in local coordinate system, respectively. Then, after separating the body by FEM, the deformations of the nodes were

$$u_f = Nq_f \tag{3}$$

where, q_f are deformations of nodes, N is shape function. The global position of P could be expressed by both reference coordinate system and floating coordinate system as follows

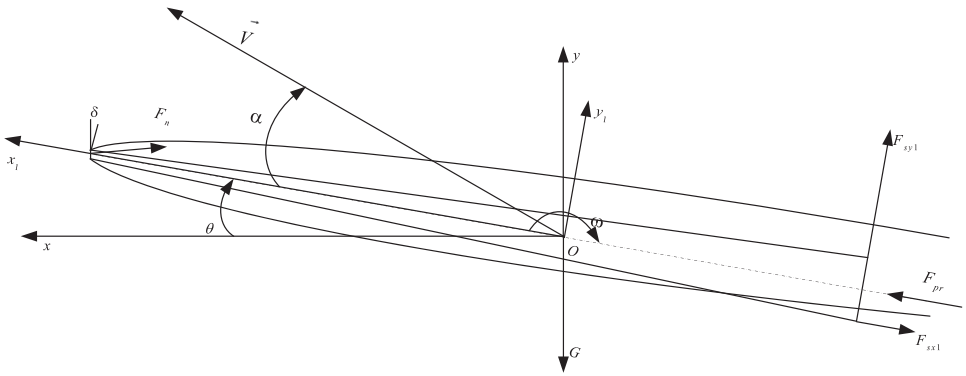

Fig. 2. Forces acting on a supercavitating projectile.

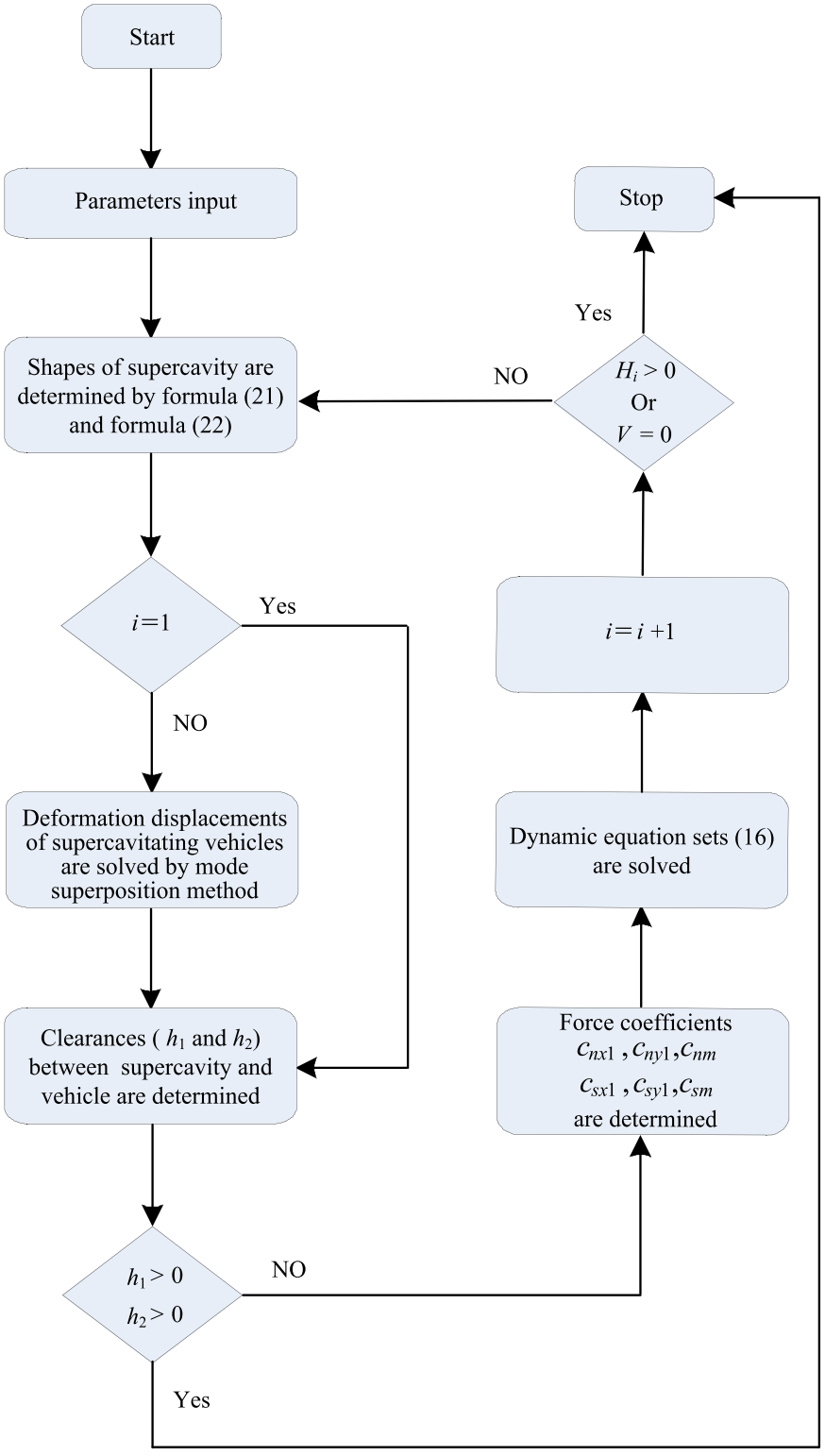

Fig. 3. Iterative calculation process of rigid-flexible-cavity coupling trajectory.

$$q^i = \begin{bmatrix} R^i \\ \theta^i \\ q_f^i \end{bmatrix} \tag{4}$$

where, θ^i are the reference coordinates with respect to rotation, q_f^i is vector of elastic coordinates.

The global velocity vector of P was obtained by derivation of formula (1)

$$\dot{r}_p^i = \dot{R}^i + \dot{A}^i u + A^i \dot{u}_f \tag{5}$$

Moreover, the global acceleration vector of P was obtained by derivation of formula (5)

$$\ddot{r}_p^i = \ddot{R} - \dot{\theta}_i^2 A_i u + \ddot{\theta}_i A^i u + A^i \ddot{u}_f^i \tag{6}$$

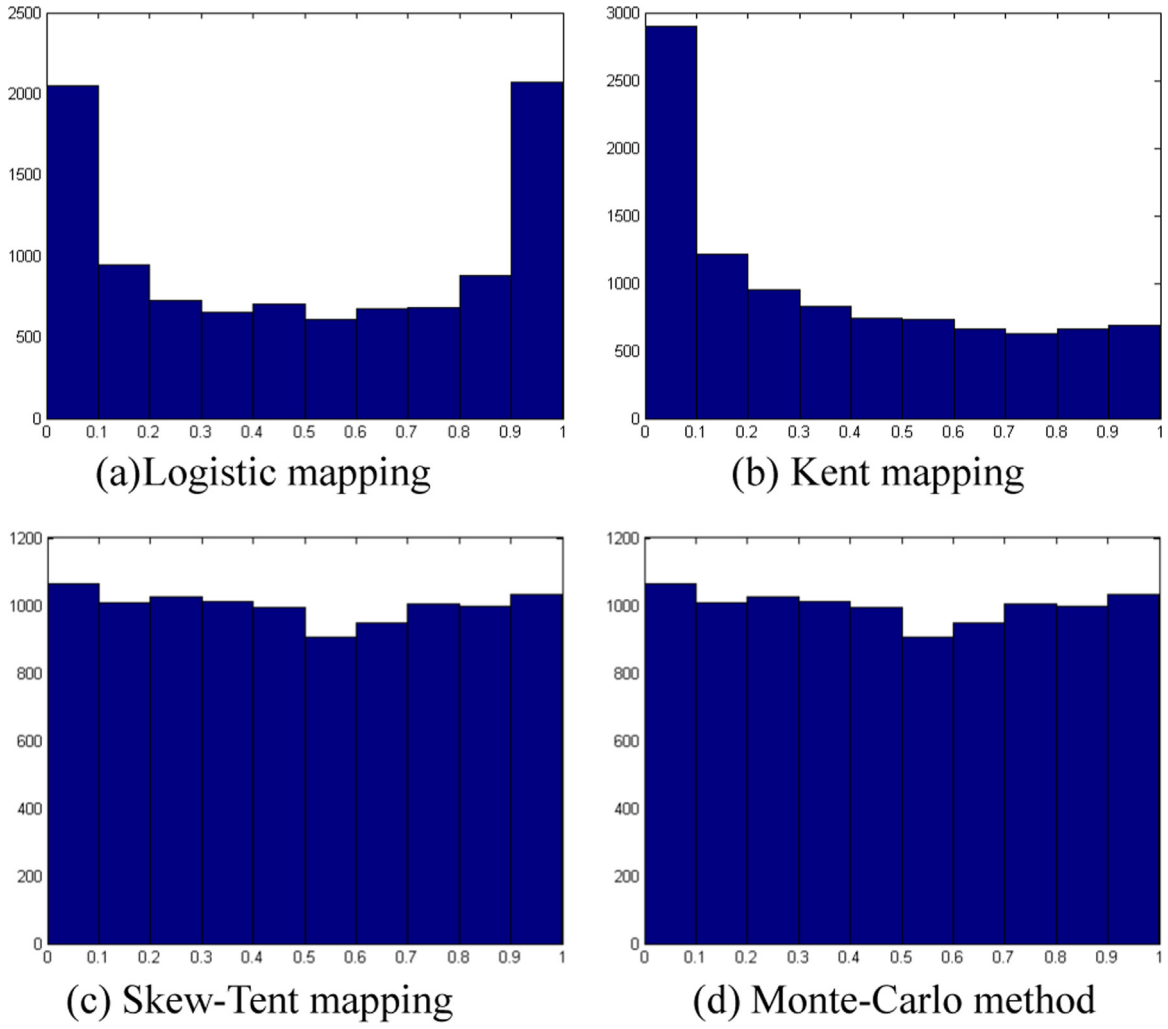

Fig. 4. Data distribution of Logistic, Kent, S-T mapping and M-C test.

Based on D'Alembert's principle and principle of virtual work, Lagrange differential equation of rigid-flexible coupled motion was established as follows (Ahmed, 2005)

$$\begin{bmatrix} m_{RR}^i & m_{R\theta}^i & m_{Rf}^i \\ & m_{\theta\theta}^i & m_{\theta f}^i \\ symmetric & & m_{ff}^i \end{bmatrix} \begin{bmatrix} \ddot{R}^i \\ \ddot{\theta}^i \\ \ddot{q}_f^i \end{bmatrix} + \begin{bmatrix} 0 & 0 & 0 \\ 0 & 0 & 0 \\ 0 & 0 & k_{ff}^i \end{bmatrix} \begin{bmatrix} R^i \\ \theta^i \\ q_f^i \end{bmatrix} + \begin{bmatrix} C_{R^i}^T \\ C_{\theta^i}^T \\ C_{q_f^i}^T \end{bmatrix} \lambda = \begin{bmatrix} (Q_e^i)_R \\ (Q_e^i)_\theta \\ (Q_e^i)_f \end{bmatrix} + \begin{bmatrix} (Q_v^i)_R \\ (Q_v^i)_\theta \\ (Q_v^i)_f \end{bmatrix} \tag{7}$$

where, m is submatrix of mass matrix, k_{ff}^i is stiffness matrix of body structure, λ is Lagrange multiplier, Q_e is external force vector, Q_v is inertia item of velocity's quadratic. The submatrix of mass matrix was solved as follows

$$M^i = \int_{V^i} \rho^i \begin{bmatrix} I \\ B^T \\ (A^i N^i)^T \end{bmatrix} \begin{bmatrix} I & B^i & A^i N^i \end{bmatrix} dV^i = \begin{bmatrix} m_{RR}^i & m_{R\theta}^i & m_{Rf}^i \\ & m_{\theta\theta}^i & m_{\theta f}^i \\ symmetric & & m_{ff}^i \end{bmatrix} \tag{8}$$

where, ρ is density of material, and B^i is given by

$$B^i = \left[\frac{\partial}{\partial \theta_1^i}(A^i u) \cdots \frac{\partial}{\partial \theta_{n_r}^i}(A^i u) \right] \tag{9}$$

Because of the high nonlinear mass matrix caused by the coupling motion of rigid motion and flexible deformation, Eq. (7) required high computational capacity to be solved.

3. Decoupled equation and flexible deformation solving method

To improve the computational efficiency to solve Eq. (7), simplified rigid-flexible coupling motion equations were established

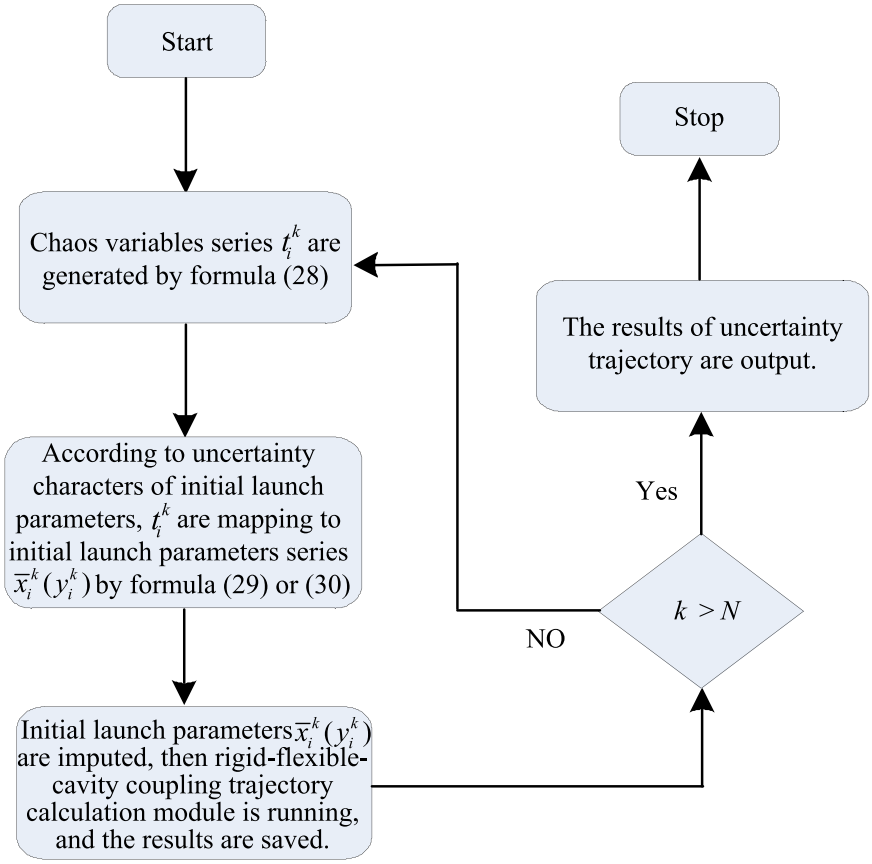

Fig. 5. Calculation process of uncertainty trajectory.

Table 1
Parameters of case 1 model.

Parameters	Values and units
Launch position x	x=0 m
Launch position y	y=−0.018 m
Initial velocity Vx_1	Vx_1=185 m/s
Initial velocity Vy_1	Vy_1=22.8 m/s
Initial Pitching angle θ	θ =−7.8°
Diameter of cavitator d_n	d_n=5.6 mm
Diameter of tail D	D=5.6 mm
Length L	L=40 mm
Density of steel ρ	ρ=2700 kg/m^3

by using linear theory of elasticity kinetics, thus formula (7) became

$$\begin{bmatrix} m_{rr}^i & m_{rf}^i \\ m_{fr}^i & m_{ff}^i \end{bmatrix}\begin{bmatrix} \ddot{q}_r^i \\ \ddot{q}_f^i \end{bmatrix} + \begin{bmatrix} 0 & 0 \\ 0 & k_{ff}^i \end{bmatrix}\begin{bmatrix} q_r^i \\ q_f^i \end{bmatrix} = \begin{bmatrix} Q_r^i \\ Q_f^i \end{bmatrix} \tag{10}$$

where, $q_r^i = [R^{iT} \quad \theta^{iT}]^T$ are position and attitudes vectors of body in global coordinate system, Q is generalized force vector, including external force, constraining force and the force related to velocity's quadratic. Suppose that elastic deformation make no difference on the rigid motion, the item $m_{rf}^i\ddot{q}_f^i$ was ignored and the above two equations became (Ahmed, 2005)

$$m_{rr}^i\ddot{q}_r^i = Q_r^i \tag{11}$$

$$m_{ff}^i\ddot{q}_f^i + k_{ff}^i q_f^i = Q_f^i - m_{fr}^i\ddot{q}_r^i \tag{12}$$

where, $m_{fr}^i = \begin{bmatrix} m_{Rf}^i & m_{\theta f}^i \end{bmatrix}$.

First, the rigid motion was solved by Eq. (11) and then the external force and inertia force were obtained and used to solve Eq. (12) to get flexible deformations. By superposition of rigid motion and flexible deformations, the motion of body was carried out. Structure dynamic Eq. (12) was solved by modal superposition method. Take the mode coordinate transformation as

$$q_f(t) = \Phi\eta(t) \tag{13}$$

where, η(t) is mode coordinate, Φ is mode matrix. Mode coordinate η(t) was substituted into vibration difference equation, and premultiplication Φ^T, then the following formula was obtained

$$M_\eta\ddot{\eta} + K_\eta\eta = F \tag{14}$$

where, $M_\eta = \Phi^T m_{ff}^i\Phi = I$, $K_\eta = \Phi^T k_{ff}^i\Phi$, $F = \Phi^T f$.

4. Rigid-flexible-cavity coupling trajectory of supercavitating projectiles

According to formula (11) and (12), rigid-flexible-cavity coupling trajectory of supercavitating projectiles can be decoupled into rigid motion and flexible deformation. In the present section, rigid-cavity coupling motion in vertical plane of supercavitating projectiles is introduced first, and then calculation flowchart of rigid-flexible-cavity coupled trajectory is presented.

4.1. Rigid-cavity coupling motions of supercavitating projectiles

Cavity envelops supercavitating projectiles, thus the external

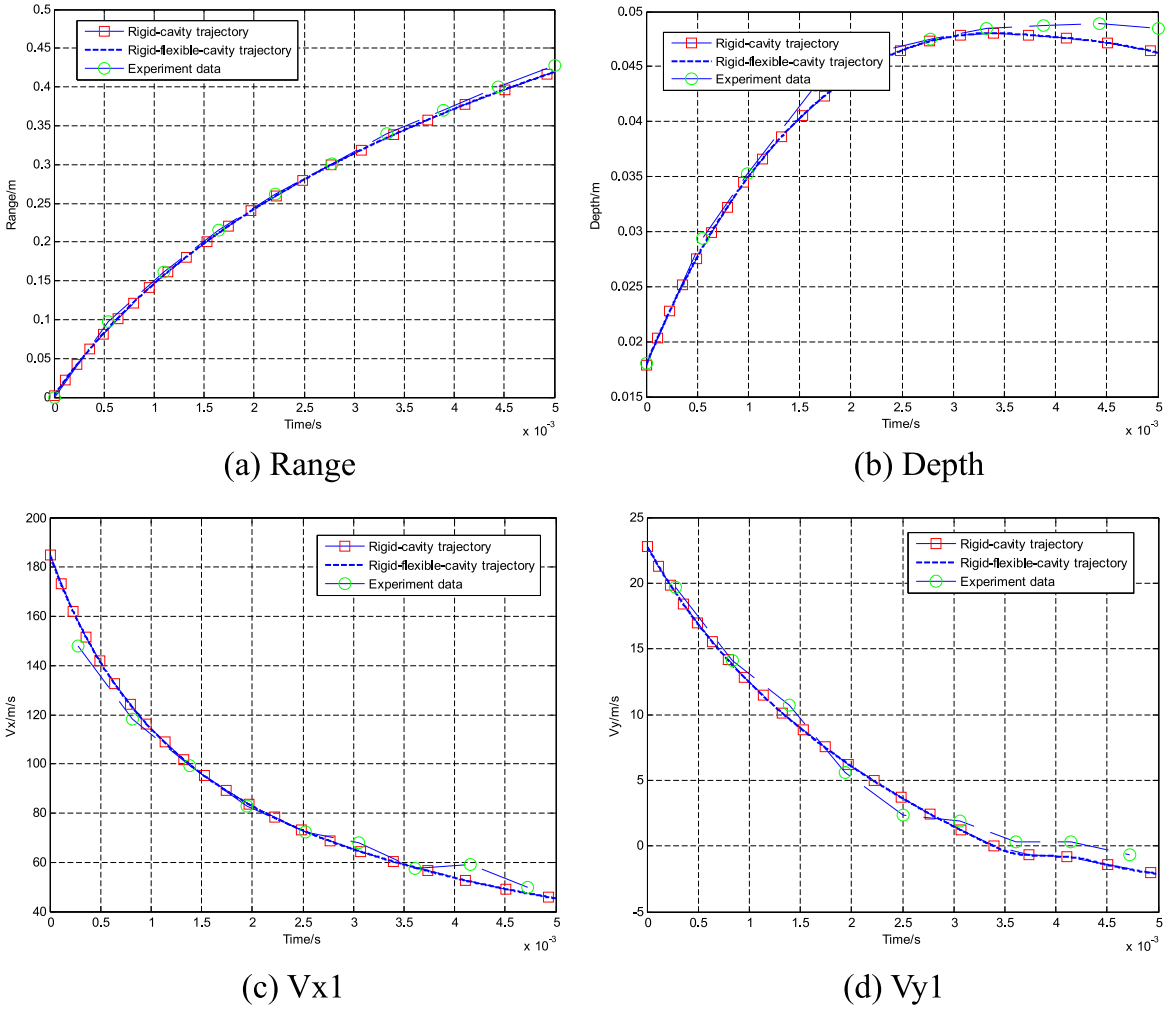

Fig. 6. Comparison of the simulation results using rigid-cavity trajectory and rigid-flexible-cavity coupling trajectory with the experimental data.

Table 2
Parameters of simulation model.

Parameters	Values and units
Launch position x	x=0 m
Launch position y	y=−5 m
Initial velocity Vx_1	Vx_1=300 m/s
Initial velocity Vy_1	Vy_1=0 m/s
Initial Pitching angle θ	θ =0°
Diameter of cavitator d_n	d_n=3.0 mm
Diameter of tail D	D=30.0 mm
Length L	L= αD (α=10,12,14)
The ratio of thrust to drag F_{pr}/F_{nx1}	F_{pr}/F_{nx1} =2
Thrust time of engine T_{pr}	T_{pr}=80 ms
Density of steel ρ	ρ=7800 kg/m^3

forces are different from those of common underwater projectiles. Supercavitating projectiles can stably operate underwater due to depend on the balance of gravity and lift force, which are provided by cavitator lift force and sliding lift force in tail. The force model is shown in Fig. 2, F_n is cavitator drag, δ is inclination angle of cavitator, $\vec{V}$ is velocity vector of projectile, α is attack angle, θ is pitch angle, ω is angular velocity which rotate with projectile centroid in vertical plane, F_{pr} is thrust of engine, F_{sy1} is lift component of sliding force, F_{sx1} is axial drag component of sliding force, G is gravity, $\boldsymbol{Oxy}$ is fixed coordinate system, $\boldsymbol{Ox_1y_1}$ is body coordinate system.

In the vertical plane, formula (11) is expressed as follows:

$$m\left(\frac{d\boldsymbol{V}}{dt}+\boldsymbol{\omega}\times\boldsymbol{V}\right)=\sum\boldsymbol{F} \tag{15a}$$

$$I_c\frac{d\boldsymbol{\omega}}{dt}=\sum M_z \tag{15b}$$

where, m is mass of projectile, $V=\{V_{x1}, V_{y1}, 0\}$ is velocity vector of projectile centroid, $\boldsymbol{\omega}=\{0, 0, \omega\}$ is angular velocity vector of projectile centroid, $F=\{F_{x1}, F_{y1}, 0\}$ is force vector, I_c is moment of inertia, $\boldsymbol{M_z}$ is moment of force. Take formula (15a) and formula (15b) integrate along x axes, and them are rewritten in detail as follows (Semenenko, 2001)

$$V\cos(\theta+\alpha)\frac{dV_{x1}}{dx}=\omega V_{y1}+\frac{1}{m}\sum F_{x1} \tag{16a}$$

$$V\cos(\theta+\alpha)\frac{dV_{y1}}{dx}=-\omega V_{x1}+\frac{1}{m}\sum F_{y1} \tag{16b}$$

$$V\cos(\theta+\alpha)\frac{d\omega}{dx}=\frac{1}{I_c}\sum M_z \tag{16c}$$

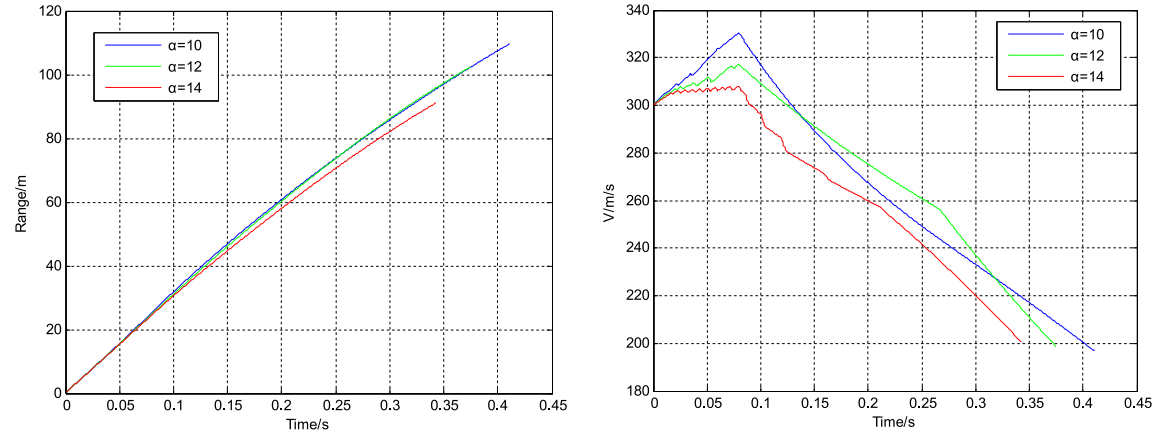

(a) Range (b) Velocity

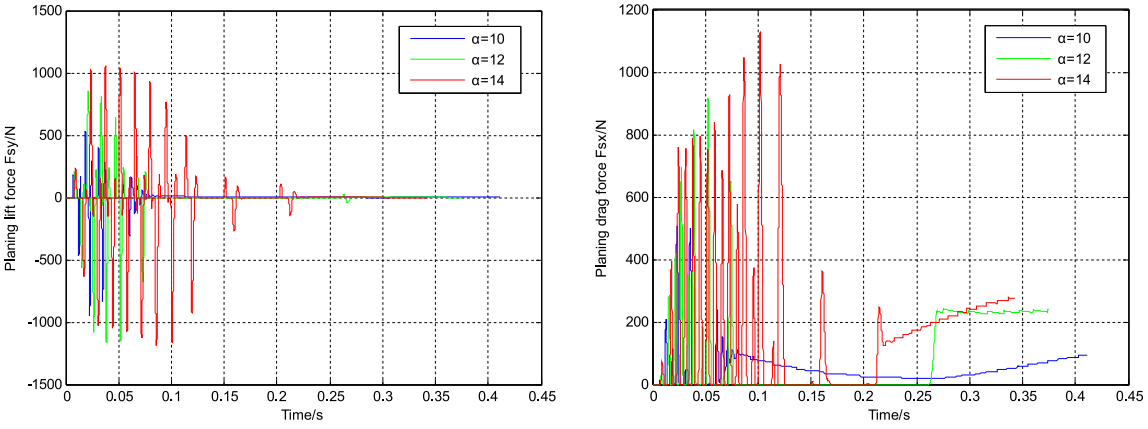

(c)Planning lift force (d)Planning drag force

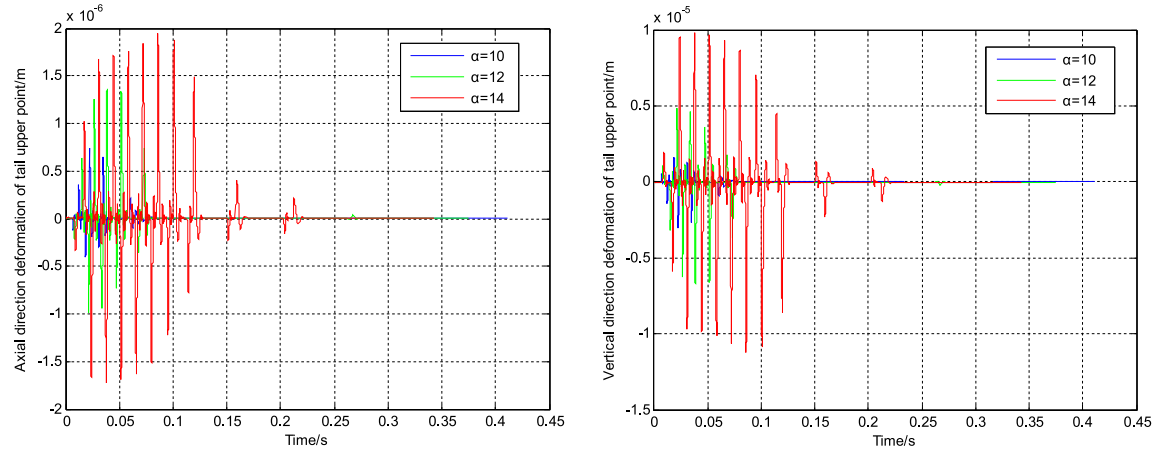

(e) axial direction deformation of tail upper point (f) Vertical direction deformation of tail upper point

Fig. 7. Comparison of the simulation results of rigid-flexible-cavity coupling trajectory under various slenderness ratios.

$$V\cos(\theta+\alpha)\frac{d\theta}{dx}=\omega \tag{16d}$$

$$\frac{dy}{dx}=\tan(\theta+\alpha) \tag{16e}$$

$$t(x)=\int_0^x \frac{ds}{V\cos(\theta+\alpha)} \tag{16f}$$

where, θ is pitch angle, α is attack angle, clockwise is defined as positive rotation, t is motion time. Force and moment equations are as follows

$$\sum F_{x1}=F_{nx1}+F_{sx1}+G_{x1}+F_{px1} \tag{17a}$$

$$\sum F_{y1}=F_{ny1}+F_{sy1}+G_{y1}+F_{py1} \tag{17b}$$

Table 3
Material properties and inherent frequencies of steel and aluminum projectiles.

Parameter	Steel projectile	Aluminum projectile
Density ρ	7800 kg/m^3	2700 kg/m^3
Young's modulus E	210 GPa	70 GPa
Poisson ratio μ	0.3	0.33
1st order frequency	1042	1033
2nd order frequency	2516	2492
3rd order frequency	4605	4559
4th order frequency	7264	7186
5th order frequency	9763	9580
6th order frequency	10,429	10,309
7th order frequency	14,033	13,861
8th order frequency	18,011	17,777
9th order frequency	18,157	17,817
10th order frequency	22,306	21,998

$$\sum M_z = M_{nz} + M_{sy1z} + M_{sx1z} \tag{17c}$$

where, F_{nx1}, F_{sx1}, G_{x1} and F_{px1} are x_1 axial components of cavitator drag, sliding force, gravity, and engine thrust respectively. F_{ny1}, F_{sy1}, G_{y1} and F_{py1} are y_1 axial components of cavitator drag, sliding force, gravity, and engine thrust. M_{nz}, M_{sx1z} and M_{sy1z} are moments of F_n, F_{sx1} and F_{sy1} respectively. Main force formulae are presented as follows. F_{nx1} and F_{ny1} are expressed by (Semenenko, 2001)

$$F_{nx1} = -\frac{\rho_{water} V^2 \pi d_n^2}{8} C_{x0}(1+\sigma)\cos(\delta-\alpha)\cos\delta \tag{18a}$$

$$F_{ny1} = -\frac{\rho_{water} V^2 \pi d_n^2}{8} C_{x0}(1+\sigma)\cos(\delta-\alpha)\sin\delta \tag{18b}$$

where, ρ_{water} is density of water, d_n is cavitator diameter, σ is cavitation number and $\sigma = 2(P_{atm}-P_c)/\rho_{water}V^2$, P_{atm} is ambient pressure and P_c is cavity pressure, C_{x0} is cavitator drag coefficient when $\sigma = 0$, and $C_{x0} = 0.8275$ when cavitator has circular disk shape (Semenenko, 2001). The formula of sliding drag force F_{sx1} is (Semenenko, 2001)

$$F_{sx1} = \frac{\rho_{water} V^2}{2} c_f(\mathrm{Re}) l\sqrt{Dh} \tag{19}$$

where, c_f is viscous drag coefficient, Re is Reynolds number, l is immersion length of projectile, h is immersion depth of projectile tail, D is diameter of projectile tail. The formula of sliding lift force F_{sy1} is (Semenenko, 2001)

$$F_{sy_1} = V\left(\rho_{water}\pi R_s^2 \frac{\bar{h}(2+\bar{h})}{(1+\bar{h})^2} V_1 + 2\rho_{water}\pi R_s^2 \frac{2\bar{h}}{1+\bar{h}} V_2\right) \tag{20a}$$

$$\bar{h} = \frac{h}{R_c - R_s} \tag{20b}$$

$$V_1 = -V_y + \omega(L - x_c) + V_{yc} \tag{20c}$$

$$V_2 = \frac{-\partial R_c}{\partial t} + \frac{\partial R_s}{\partial t} \tag{20d}$$

where, R_s is tail radius of projectile, R_c is the radius of supercavity, V_y is vertical velocity of projectile centroid, L is length of projectile, x_c is distance from cavitator to projectile centroid, V_{yc} is lateral velocity of cavity axis, V_2 is boundary velocity of cavity.

Formulae (19) and (20) show that the components of sliding force are related to immersion depth, immersion length and shape change velocity of cavity at each time. To obtain accurate sliding force, accurate cavity shape needs to be obtained at each time. Based upon Logvinovich independence expansion principle of the supercavity section, the supercavity radius was calculated as follows (Logvinovich, 1972)

$$S(\tau, t) = \frac{\pi d_n^2}{4} + k(t-\tau)\frac{A d_n}{4} V\sqrt{C_{x0}} - \frac{k}{\rho_{water}}\int_\tau^t du \int_\tau^u \Delta P(\tau, v)dv \tag{21}$$

where, $S(\tau, t)$ is cavity area in τ section at t time, $k = 4\pi/A^2$, $A = \sqrt{\ln 1/\sigma}$, and ΔP is pressure difference between ambient pressure P_{atm} and cavity pressure P_c. Directional effect of cavitator and floating deformation of cavity tail are considered, and the center of cavitator $z_{o'}$ in τ section at t time is expressed as (Logvinovich, 1972)

$$z_{o'} = z(t-\tau) - \frac{g}{\pi V^2}\int_0^x \frac{Q(x)}{R_c^2(x)}dx - \frac{8F_{ny}}{\rho\pi V^2 R_n^2} R_n\left(0.46 - \sigma + \frac{x}{L_c}\right) \tag{22}$$

where, $Q(x)$ is cavity volume, F_{ny} is cavitator lift, R_n is cavitator radius, x is the distance from cavitator to $z_{o'}$, L_c is cavity length.

Formula (21) shows that unsteady cavity shape is relative to current cavitation number, current velocity, and current pressure difference. So shape and position of supercavity in motion process were obtained through iterative calculation at time t first, and then iterative calculation on cavity length at current time.

4.2. Calculation flowchart of rigid-flexible-cavity coupling trajectory of supercavitating projectiles

Because hydrodynamic forces the projectile suffered are related to current cavity, current state parameters, and flexible deformation of projectile, motion of supercavitating projectile is a rigid-flexible-cavity coupling iteration calculation process. Following Fig. 3 shows the calculation flowchart at each iteration cycle, where i is iteration numbers, c_{nx1} and c_{ny1} are coefficients of cavitator drag components, c_{sx1} and c_{sy1} are coefficients of sliding force components, c_{nm} and c_{sm} are moment coefficients of cavitator drag and sliding force. Depth $H_i > 0$ indicates that projectile fly off water surface. $h_1 > 0$ and $h_2 > 0$ indicate ring immersion of projectile. The iterative process stops when above $h_1 > 0$ and $h_2 > 0$ arise or $V = 0$.

5. Uncertainty rigid-flexible-cavity coupling trajectory calculations

5.1. Uncertainty variables

Considering the various uncertainties of initial parameters of the launch of supercavitating projectile, uncertainty trajectory analysis was required. The uncertain parameters of the launch could be described by truncated probabilistic variables and non-probabilistic interval variables due to their data samples are sufficient or non-sufficient.

5.1.1. Truncated random variables

When the accurate probability distributions of uncertain variables could be obtained, and uncertain variables were generally bounded in practical engineering, it is more appropriate that infinite probabilistic distribution variables were substituted by truncated probability distribution variables in engineering.

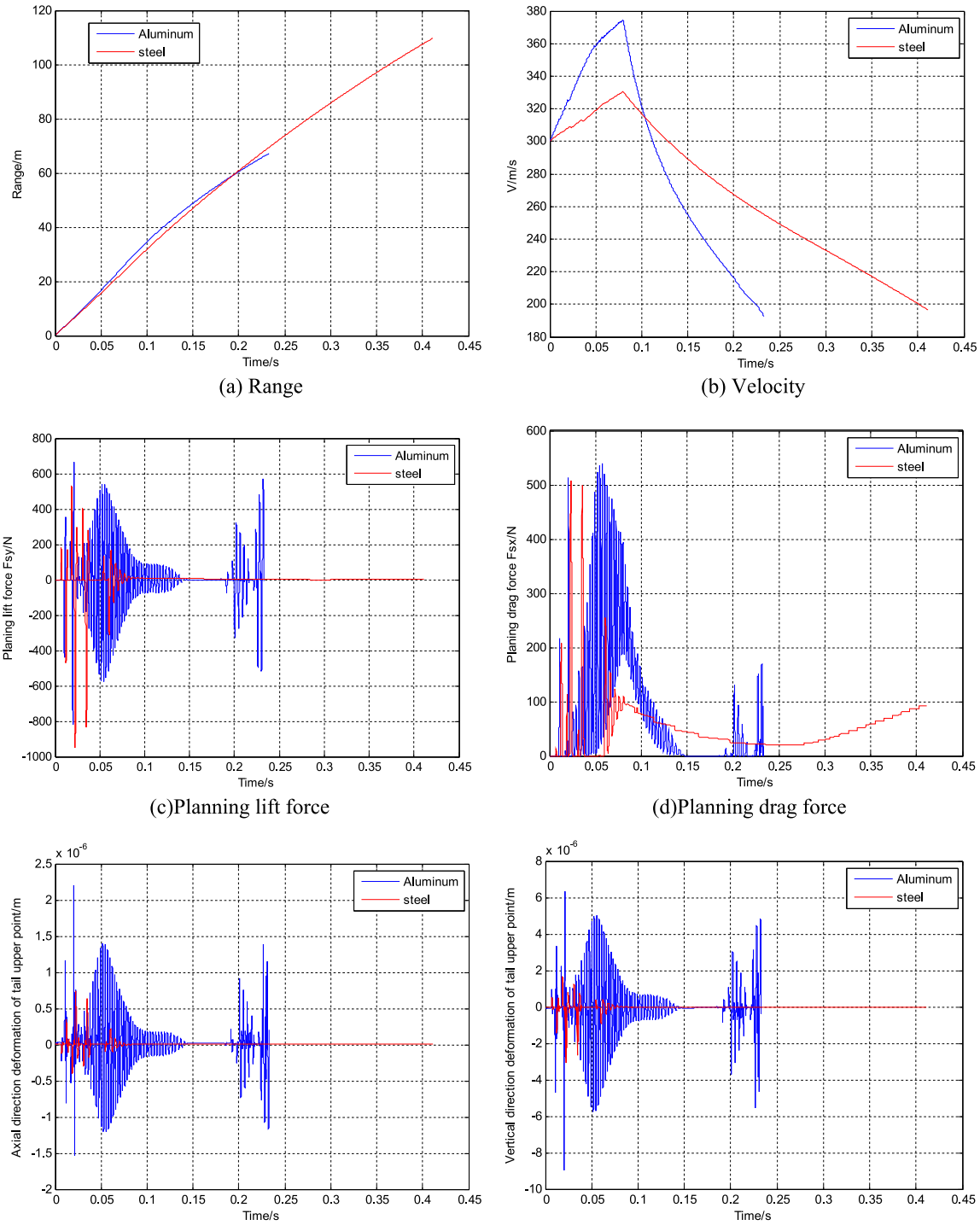

(a) Range (b) Velocity

(c)Planning lift force (d)Planning drag force

(e) axial direction deformation of tail upper point (f) Vertical direction deformation of tail upper point

Fig. 8. Comparison of the simulation results of rigid-flexible-cavity coupling trajectory between steel projectile and aluminum projectile.

Assume $\bar{X}_i$ is truncated probability variable with interval $[a_i,b_i]$, its Probability Density Function (PDF) $f_X(\bar{X}_i)$ and Cumulative Probability Distribution Functions (CDF)$F_X(\bar{X}_i)$ are as follows

$$f_X(\bar{X}_i) = \frac{f_X(X_i)}{F_X(b_i) - F_X(a_i)} \tag{23}$$

$$F_X(\bar{X}_i) = \frac{1}{F_X(b_i) - F_X(a_i)}(F_X(x) - F_X(a_i)) \tag{24}$$

where, $f_X(X_i)$ is PDF of ith continuous random variable X_i, and $F_X(X_i)$ is CDF of ith continuous random variable X_i.

5.1.2. *Interval variables*

When data samples of uncertainty parameters are not sufficient in engineering, the accurate probability distribution cannot be calculated, but the upper and lower bounds of uncertainty variables could be easily obtained. Therefore, non-probabilistic interval variables should be adopted to describe above uncertainty parameters as follows (Ling et al., 2011)

Table 4
Main parameters of supercavitating projectile.

Parameters	Values
Launch position x	$x=0$
Launch position y	$y=-25$ m
Initial velocity Vx_1	$Vx_1=600$ m/s
Initial velocity Vy_1	$Vy_1=0$
Angular velocity ω	$\omega=2$ rad/s
Pitching angle θ	$\theta=0$
The ratio of thrust to drag F_{pr}/F_{nx1}	$F_{pr}/F_{nx1}=2$
Thrust time of engine T_{pr}	$T_{pr}=80$ ms
Diameter of cavitator d_n	$d_n=3$ mm
Diameter of tail D	$D=30$ mm
Density of steel ρ	$\rho=7800$ kg/m^3

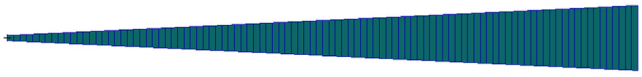

Fig. 9. FEM model of supercavitating projectile.

Table 5
Front 10 order inherent frequency.

Mode	Inherent frequency (Hz)
1	2.04×10^3
2	4.79×10^3
3	8.59×10^3
4	1.33×10^4
5	1.89×10^4
6	2.08×10^4
7	2.51×10^4
8	3.19×10^4
9	3.84×10^4
10	3.91×10^4

$$Y_i \in Y_i^{\mathrm{I}} = \left[Y_i^l, Y_i^u \right] \tag{25}$$

where, Y_i^{I} is the interval of interval variable Y_i, Y_i^l is the lower bound of Y_i, Y_i^u is the upper bound of Y_i.

5.2. Uncertainty variables generated by Chaos method

Considering the random, ergodicity and uniformity of chaos variables, chaos method was used to simulate uncertain trajectory. Ergodicity and uniformity of chaotic variables formed by different chaos mapping iteration formulae were compared first. Logistic map equation, Kent map formula, and Skew-Tent map formula are as follows.

a) Logistic map equation (Walters, 1982)

$$t_i^{k+1} = \mu t_i^k \left(1 - t_i^k\right) \quad i = 1, 2, \ldots, n \quad k = 1, 2, \ldots, N \tag{26}$$

where, t_i^k is ith chaotic variable at kth iteration. Initial value $0 < t_i^0 < 1$, and Logistic mapping is under chaotic state when $\mu = 4$. Interval [0, 1] is the invariability set of Logistic mapping.

b) Kent map formula (Chua et al., 1990)

$$\begin{cases} kt_i^k = t_i^k/\beta 0 \le t_i^k \le \beta \\ kt_i^k = \left(1 - t_i^k\right)/(1-\beta)\beta < t_i^k \le 1 \end{cases} \tag{27}$$

where, t_i^k is chaotic variable formed by Logistic map, and then Kent map chaos variables are formed through formula (27). When parameter $\beta \in (0, 1)$, Kent map is under chaotic state, and interval [0, 1] is the invariability set of Kent map.

c) Skew-Tent map formula (Hasler and Maistrenko, 1997)

$$t_i^{k+1} = \begin{cases} t_i^k/at_i^k \in (0, a] \\ (t_i^k - 1)/(a-1)t_i^k \in (a, 1) \end{cases} \quad a \in (0, 1) \tag{28}$$

The case $a = 0.5$ corresponds to Tent map. When $a \in (0, 1)$, Skew-Tent is under chaotic state, and interval [0, 1] is the invariability set of Skew-Tent map.

The uniformity of tracking point formed by the above three different chaos map was checked as follows. Distributions of tracking point formed by Logistic map, Kent map, Skew-Tent map, and Monte-Carlo method are shown in Fig. 4. Both the number of tracking points and random numbers of Monte-Carlo method were 10,000. Tracking points of three different maps had the same initial value of 0.1. In Kent map β was 0.4, in Skew-Tent map a was 0.3. Fig. 4 shows that Skew-Tent has the best uniformity, which is closest to the one of Monte-Carlo method. Moreover, Skew-Tent map does not need to form additional abandon points, therefore it is best that tracking points formed by Skew-Tent chaos map simulate the uncertainty trajectory.

5.3. Simulation flowchart of uncertainty trajectory

The simulation flowchart of uncertainty trajectory is shown in Fig. 5. Chaotic variables series t_i^k were generated first by Skew-Tent mapping formula (28). Then, t_i^k were mapped to initial launch parameters series. If the launch parameters were truncated probability distribution variables $\bar{x}_i^k$, its mapping formula was as follows

$$\bar{x}_i^k = F_X^{-1}\left(t_i^k\left(F_X(b_i) - F_X(a_i)\right) + F_X(a_i)\right) \tag{29}$$

If the launch parameters were non-probabilistic interval variables y_i^k, its map equation was

$$y_i^k = Y_i^l + t_i^k\left(Y_i^u - Y_i^l\right) \tag{30}$$

Third, $\bar{x}_i^k$ and y_i^k were entered into rigid-flexible-cavity coupling trajectory calculation flowchart shown in Fig. 3, and the results of trajectory saved. Finally, if the number of track point were greater than requested number N, the simulation stopped, otherwise simulation continued.

6. Numerical examples

The following are three numerical examples. The first example presented in this section is used to validate calculation algorithm of rigid-flexible-cavity coupling trajectory. The second example is used to investigate the effect of flexible deformation of projectile on coupling trajectory. The final numerical example of projectile model is from engineering practice and its rigid-flexible-cavity coupling trajectory and uncertain trajectory results were presented.

6.1. Example for validation

To validate the calculation algorithm of rigid-flexible-cavity coupling trajectory, the case 1 of the experimental model described in (Mirzaei et al., 2015) was selected; the simulation model's parameters are listed in Table 1. Fig. 6 compares the calculated rigid-cavity and rigid-flexible-cavity coupling trajectories with the experimental ones. The simulation results based on the

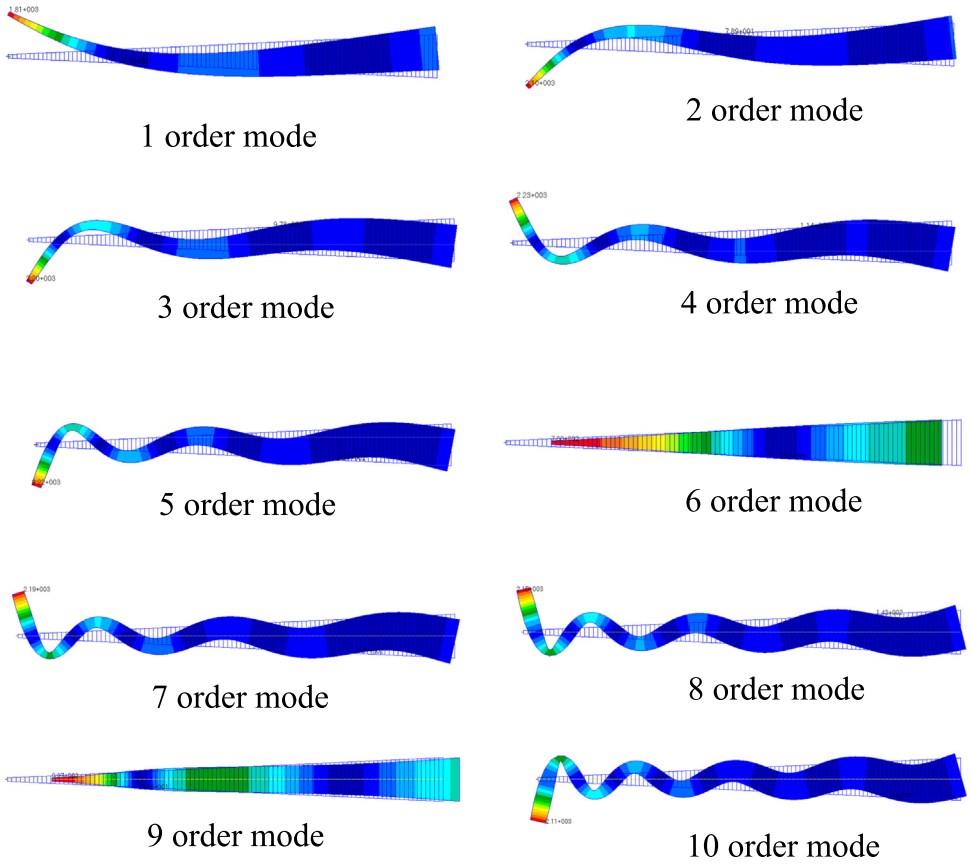

Fig. 10. Front 10 order mode shapes.

two trajectory patterns are consistent; moreover, the results well agree with the experimental data, and the error lies within the acceptable range. Thus, the correctness of the calculation approach of rigid-cavity trajectory and rigid-flexible-cavity coupling trajectory was validated. Because the short trajectory simulation time span (duration of milliseconds), the effect of projectile flexibility on trajectory can be neglected, and this explains the identical calculation results of the trajectory with or without considering flexibility.

6.2. *Effect of flexibility*

To investigate the effect of flexible deformation of projectile on coupling trajectory, the variation of the resultant coupling trajectory was investigated by varying two important flexibility parameters – slenderness ratio and Young's modulus.

6.2.1. *Effect of slenderness ratio*

Table 2 lists the parameters of the supercavitating projectile model in the simulation example, where $\alpha = L/D$ is slenderness ratio and it is set as 10, 12 and 14 for comparison. The simulation results in Fig. 7 show that with greater slenderness ratio, the tail force becomes greater, and the tail deformation of projectile is larger. Moreover, with greater slenderness ratio, the range becomes shorter and the speed reduces more rapidly because as the slenderness ratio increases, the mass of projectile increases, the degree of speed increment in the early period decreases, and the tail drag force increases, thereby resulting in a reduced motion range and more rapidly declined speed.

6.2.2. *Effect of Young's modulus*

To study the effect of Young's modulus on flexible deformation of projectile and coupling trajectory, the supercavitating projectile model ($\alpha = 10$) in Table 2 was used, while different materials (i.e. steel and aluminum) were used. Table 3 lists the material properties and the inherent frequencies of the first 10 orders. Fig. 8 compares the simulation results of coupling trajectory between steel projectile and aluminum projectile. One can observe that the range of aluminum projectile is shorter than that of steel projectile; although the speed of aluminum projectile is increased, the declination is faster. The tail force and the deformation of aluminum projectile are greater than those of the steel one. Therefore, the influence of aluminum projectile characterized by larger flexibility on coupling trajectory is greater than that of steel projectile.

6.3. *Engineering example*

Supercavitating projectile was made of steel; following Table 4 lists initial parameters of launch and main dimensional parameters.

6.3.1. *Calculation of rigid-flexible-cavity coupling trajectory*

Before calculating coupling trajectory, mode analysis results of supercavitating projectile are presented first, and they will be used to solve flexible deformations in coupling motion process. The finite element model of supercavitating projectile is shown in Fig. 9,

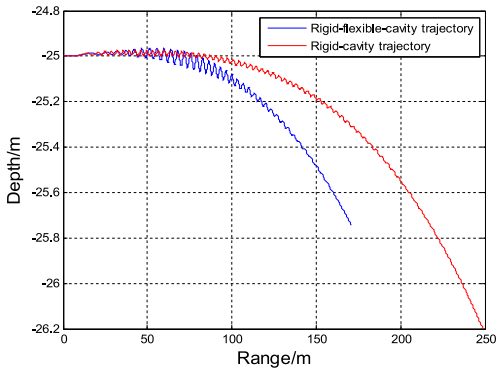

(a)Trajectory curve

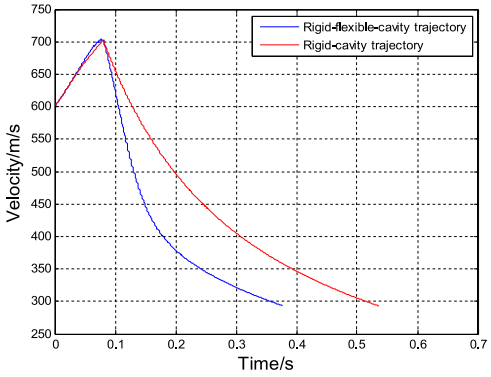

(b) Velocity

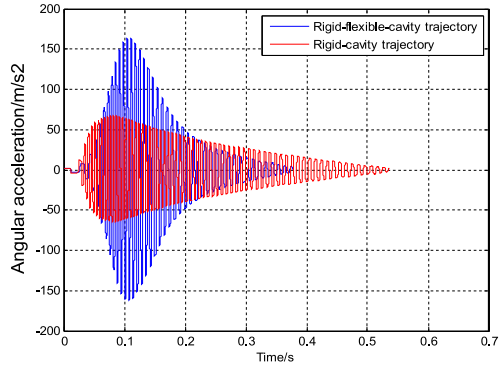

(c)Angular acceleration

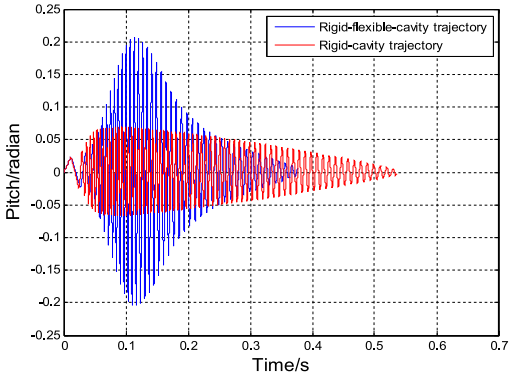

(d) Pitch angle

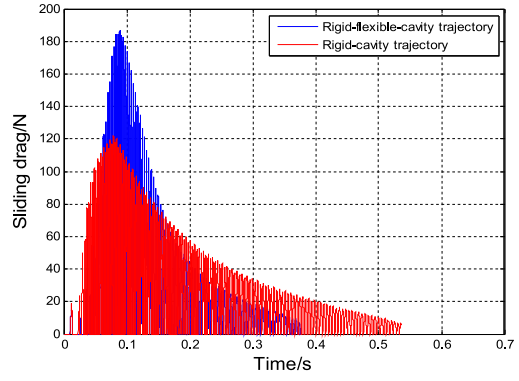

(e) Sliding drag

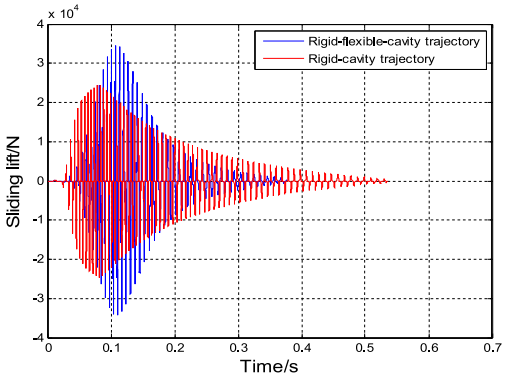

(f) Sliding lift

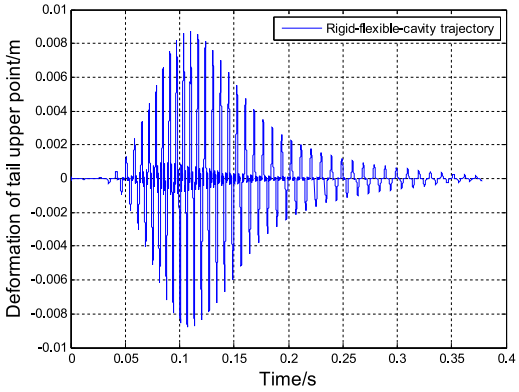

(g) x direction deformation of tail upper point

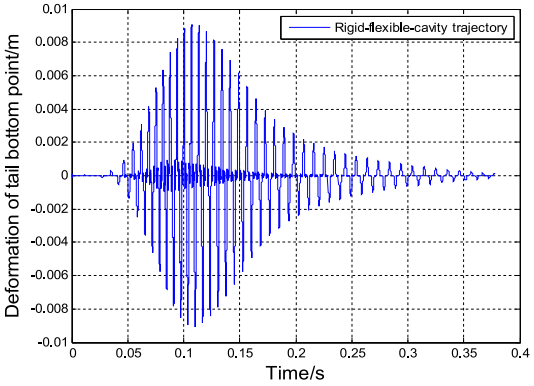

(h) x direction deformation of tail bottom point

Fig. 11. Comparison of the results between two trajectories.

Table 6
Parameters of supercavitating projectile.

Parameters	Parameters styles	Values
Initial velocity V_{x_1}	Interval variables	$V_{x_1} \in [-250, 350]$ m/s
Angular velocity ω	Truncated normal distribution variable	$\mu_\omega = 0,\ \sigma_\theta = 2/3\text{rad/s}\,\omega \in [-2, 2]$ rad/s
Pitching angle θ	Truncated normal distribution variable	$\mu_\theta = 0,\ \sigma_\theta = 0.1^\circ/3, \theta \in [-0.1^\circ, 0.1^\circ]$

in which the number of discrete elements is 100. The Front 10 order inherent frequencies are listed in Table 5, and the corresponding mode shape are shown in Fig. 10. The Front 10 order modes were used to solve flexible deformations of supercavitating projectile.

Following Fig. 11 compares the results of rigid-cavity trajectory and that of rigid-flexible-cavity trajectory. Big differences between trajectories can be highlighted. The motion distance of rigid-cavity trajectory is larger than that of rigid-flexible-cavity trajectory, because flexible deformations consume parts of kinetic energy and the velocity declines quickly. The angle acceleration, pitch angle, sliding drag, and sliding lift in rigid-flexible-cavity trajectory are larger than that in rigid-cavity trajectory. This is because the flexible deformations of tail point, which are shown in Fig. 11(g)–(h) and the deformation values cannot be ignored, thus they obviously influence sliding force, and then influence the motion process and state parameters of supercavitating projectile. Therefore, the flexible deformations of supercavitating projectile need to be considered in trajectory calculation.

6.3.2. Calculation of uncertainty rigid-flexible-cavity coupling trajectory

The initial parameters of the launch and dimensional parameters were the same as that of Table 4, while uncertainty parameters are listed in Table 6; their data samples are from experiments and engineers.

The results of coupling trajectory curve sets, distribution of impact points, depth distribution of impact points, and range distribution of impactf points are shown in Fig. 12. The dispersion degree of depth distribution of impact points is small, but that of range distribution of impact points is large.

7. Conclusions

In this paper, the calculation flowchart of rigid-flexible-cavity coupling trajectory is presented and chaos method is used to perform rigid-flexible-cavity coupling uncertainty trajectory simulation. The results show that there is a big difference between rigid-flexible-cavity trajectory and rigid-cavity trajectory, and the flexible deformations of supercavitating projectiles during underwater operation at high velocity need to be considered. In addition, the initial uncertainty parameters of the launch have great influence on range distribution.

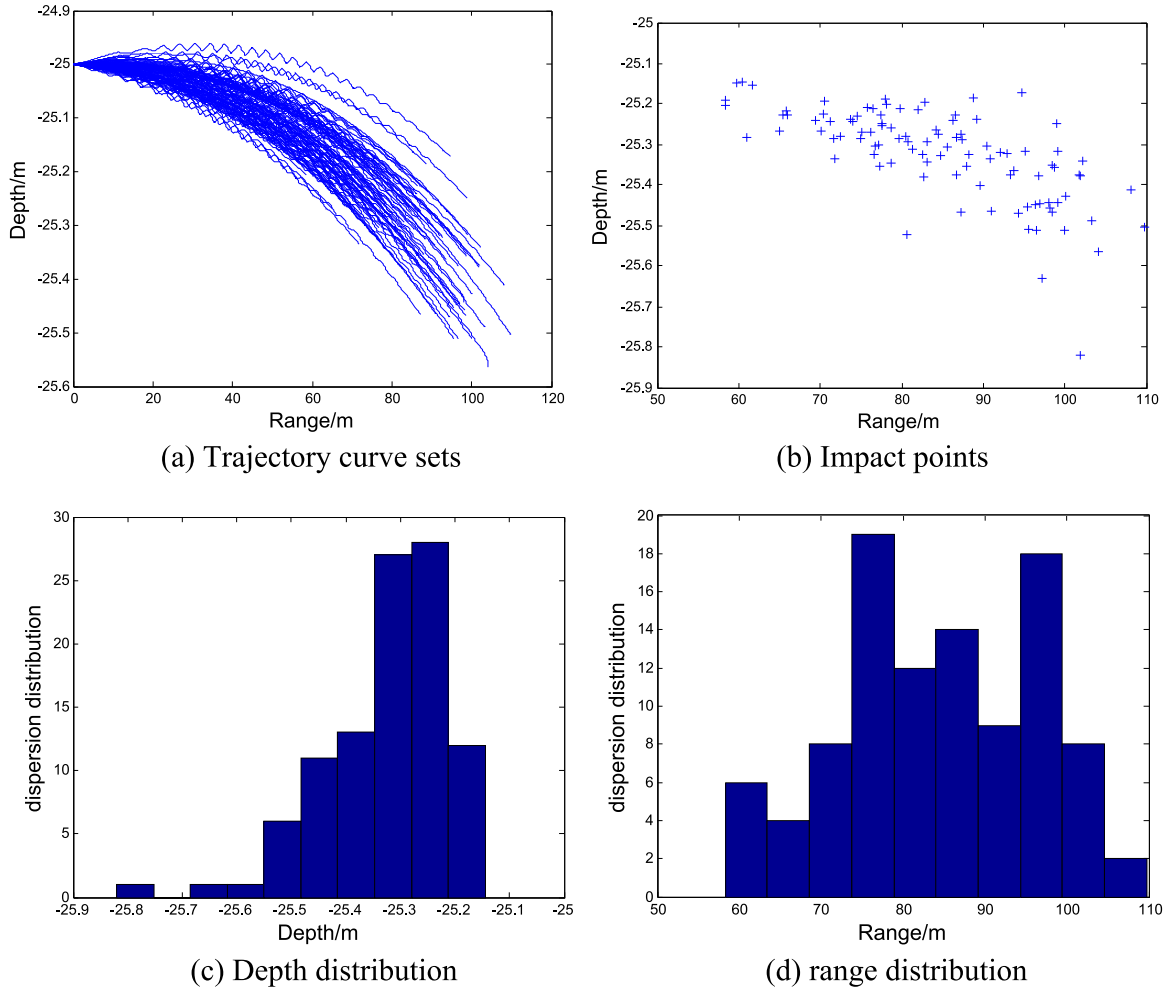

Fig. 12. Results of uncertainty trajectory.

Acknowledgements

This work was supported by the National Natural Science Foundation of China (Grant No. 51305421), and the Development of Science and Technology Project of Jilin Province (Grant No. 20140520137JH).

References

Ashley, S., 2001. Warp-drive underwater. Sci. Am. 30 (4), 70–79.
Ben-Haim, Y., 1994. A non-probabilistic concept of reliability. Struct. Saf. 14 (4), 227–245.
Choi, Jou-Young, Ruzzene, Massimo, Bauchau, Olivier A., 2004. Dynamic analysis of flexible supercavitating vehicles using modal-based elements. Simulation 80 (11), 619–633.
Chua, L.O., Yao, Y., Yang, Q., 1990. Generating randomness from chaos and constructing chaos with desired randomness. Int. J. Circuit Theory Appl. 18, 215–240.
Elishakoff, I., 1995. Essay on uncertainties in elastic and viscoelastic structure: from A.M. Freudenthal's criticisms to modern convex modeling. Comput. Struct. 56 (6), 871–895.
Harkins, T.K. Hydroballistics: Development, Theory and Some Test Results. In: 19th International Symposium on Ballistics, Interlaken, Switzerland, 7–11 May 2001.
Hasler, M., Maistrenko, Y.L., 1997. An introduction to the synchronization of chaotic systems: coupled skew tent maps. IEEE Trans. Circuits Syst.-I 44 (10), 856–866.
Kulkarni, Salil S., Pratap, Rudra, 2000. Studies on the dynamics of a supercavitating projectile. Appl. Math. Model. 24, 113–129.
Ling, Zhou, Weiguang, An, Hongguang, Jia, 2011. Definition and solution of reliability comprehensive index of super-ellipsoid convex set. Acta Aeronaut. Astronaut. Sin. 32 (11), 2025–2035.
Logvinovich, G.V. Hydrodynamics of flows with free boundaries. Translated from the Russion (NASA-TT-T-658), US Department of Commerce, Washington D C, 1972: 103–133.
Mirzaei, Mojtaba, Alishahi, Mohammad Mehdi, Eghtesad, Mohammad, 2015. High-speed underwater projectiles modeling: a new empirical approach. J. Braz. Soc. Mech. Sci. Eng. 37, 613–626.
Richard Rand, Rudra Pratap, Deepak Ramani, Jeffery Cipdla, Ivan Kirschner. Impact dynamics of a supercavitating underwater projectile. Proceedings of ASME Design Engineering Technical Conferences, Sacramento, California 14–17 September 1997.
Ruzzene, M., Soranna, F., 2004. Impact dynamic of elastic stiffened supercavitating underwater vehicles. J. Vib. Control 10, 243–267.
Ruzzene, M., Kamada, R., Bottasso, C.L., Scorcelletti, F., 2008. Trajectory optimization strategies for supercavitating underwater vehicles. J. Vib. Control 14 (5), 611–644.
Ruzzene, Massimo, 2004. Dynamic buckling of periodically stiffened shells: application to supercavitating vehicles. Int. J. Solids Struct. 41, 1039–1059.
Semenenko, V.N., 2004. Calculation of two-dimensional unsteady supercavities at arbitrary time dependence. Int. J. Fluid Mech. Res. 31 (6), 621–632.
Semenenko, V.N., Dynamic processes of supercavitation and computer simulation. RTO AVT Lecture Series on Supercavitating Flows, Von Karman Institute, Brussels, Belgium, February 2001.
Shabana, Ahmed A., 2005. Dynamics of Multibody System, Third edition. Cambridge University Press, London.
Walters, P., 1982. An Introduction to Ergodic Theory. Springer-Veringer, New York.
Xiao, Ning-Cong, Li, Yan-Feng, Yang, Yuanjian, Yu, Le, Huang, Hong-Zhong, 2014. A novel reliability method for structural systems with truncated random variables. Struct. Saf. 50, 57–65.
Yunhua, Jiang, Weiguang, An, Ling, Zhou, 2011. Trajectory stochastic characteristics analysis of supercavitation projectile with stochastic parameters. Chin. J. Comput. Mech. 28 (1), 25–30.
Zhang, Xiaoyu, Han, Yuntao, Bai, Tao, Wei, Yanhui, Kemao, Ma, 2015. H_{∞} controller design using LMIs for high-speed underwater vehicles in presence of uncertainties and disturbances. Ocean Eng. 104, 359–369.